Investigating motion-induced signal corruption in steady-state diffusion MRI

Benjamin C. Tendler[1*], Wenchuan Wu[1], Karla L. Miller[1], Aaron T. Hess[1]
[1]Centre for Integrative Neuroimaging, FMRIB, Nuffield Department of Clinical Neurosciences, University of Oxford, Oxford, UK

*Corresponding Author. Email: benjamin.tendler@ndcn.ox.ac.uk

Abstract

Purpose: Diffusion-weighted steady-state free precession (DW-SSFP) is a diffusion imaging sequence achieving high SNR efficiency and strong diffusion-weighting. A key challenge for in vivo DW-SSFP is the sequence's severe motion sensitivity, currently limiting investigations to low or no motion regimes. Here we establish a framework to both (1) investigate and (2) correct for the impact of subject motion on the DW-SSFP signal.

Theory and Methods: An extended phase graphs (EPG) representation of the DW-SSFP signal was established incorporating a motion operator describing rigid body and pulsatile motion. The representation was validated using Monte Carlo simulations, and subsequently integrated into a data fitting routine for motion estimation and correction. The fitting routine was evaluated using both simulations and experimental 2D low-resolution single-shot timeseries DW-SSFP data acquired in a human brain, with a tensor reconstructed from the motion-corrected experimental DW-SSFP data.

Results: The proposed EPG-motion framework gives excellent agreement to complementary Monte Carlo simulations, demonstrating that diffusion coefficient estimation is robust over a range of motion and SNR regimes. Tensor estimates from the motion-corrected experimental DW-SSFP data give excellent visual agreement to complementary DW-SE data acquired in the same subject.

Conclusion: Temporal information capturing the evolution of the DW-SSFP signal can be used to retrospectively (1) estimate subject motion and (2) reconstruct motion-corrected DW-SSFP data. Open-source software is provided, facilitating future investigations into the impact of subject-motion on DW-SSFP acquisitions.

Keywords: Diffusion MRI, Motion Correction, Steady-State Diffusion, Diffusion-Weighted Steady-State Free Precession, Extended Phase Graphs, in vivo

Introduction

Diffusion-weighted steady-state free precession (DW-SSFP)[1–4] is an alternative to the diffusion-weighted spin-echo (DW-SE)[5] for diffusion MRI investigations. Its diffusion encoding module consists of a single diffusion gradient and RF pulse per TR (Figure 1), with signal-forming mechanisms that offer several advantages for diffusion imaging. To date, DW-SSFP has demonstrated high-SNR efficiency and strong diffusion-weighting[6], with growing evidence that resulting image contrast may be highly sensitive to microstructural features[7,8].

In diffusion MRI, applied diffusion encoding gradients sensitise signals to the microscopic (μm) scale, with diffusion processes in tissue leading to attenuation of signal magnitude[5]. Measured signals are also intrinsically sensitive to subject motion, with small tissue displacements (e.g. arising from bulk, pulsatile, or respiratory induced motion) leading to changes in signal phase[9,10]. The presence of motion-induced artefacts in reconstructed images is strongly dependent on the incorporated readout scheme. The combination of phase-inconsistent k-space data associated with segmented readouts can give rise to considerable artefacts in reconstructed magnitude images[11], impacting the quantification of diffusion attenuation. DW-SE sequences incorporating single-shot readouts are typically considered motion robust[12,13], with a notable exception of motion induced 'dropout' arising when the echo is displaced from the k-space field of view (FOV)[14–16].

DW-SSFP is typically implemented as a 3D sequence with a short TR (~20 to 40 ms), with image formation dependent on a heavily segmented (or single line) readout. Whilst providing the benefit of minimal geometric distortions, previous work has demonstrated that the DW-SSFP acquisitions are highly sensitive to both rigid body (head translation/rotation) and pulsatile (i.e. arising from the cardiac cycle) motion[17–22]. At present, the motion-sensitivity of DW-SSFP limits investigations to low (cartilage[23,24], peripheral nerves[25]) or no (post-mortem[6]) motion imaging regimes.

Several motion-correction methods have been previously established to address motion artefacts arising from segmented diffusion MRI acquisitions. Typically these methods introduce navigator echoes[26,27] or 'self-navigating' readouts (e.g. PROPELLER[28,29], SNAILS[30,31]) to the sequence, or exploit sensitivity encodings (e.g. MUSE[32], MUSSELS[33]) to estimate and correct for motion-induced phase inconsistencies across acquired k-space segments. These techniques have demonstrated considerable promise for the DW-SE sequence, raising a simple question – can we directly translate an existing method to correct for subject motion in DW-SSFP?

Unfortunately, a key challenge for DW-SSFP is the specialised nature of how motion corrupts the signal associated with the underlying magnetisation distribution (i.e. independent of the readout scheme and k-space FOV). Specifically, whilst subject motion corrupts the DW-SE signal phase, in DW-SSFP subject motion corrupts both the signal phase *and* magnitude[3] (Fig. 2). Whilst conventional motion-correction techniques can be incorporated to attenuate artefacts associated with the sequence's segmented readout[17–21], we require further extensions to account for the specific signal forming mechanisms of DW-SSFP.

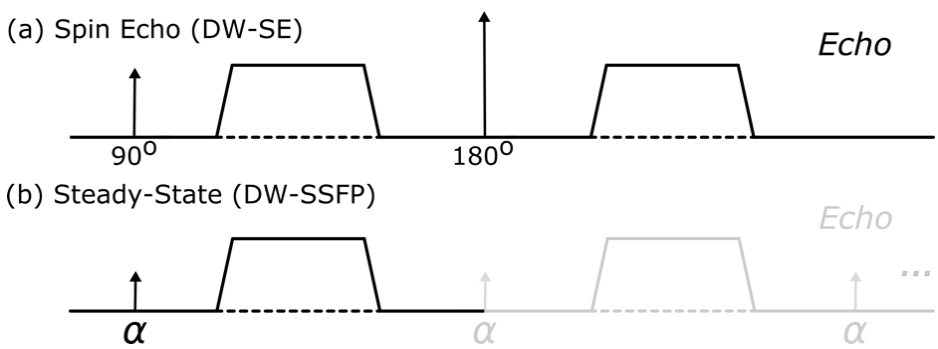

Figure 1: **Diffusion encoding.** Here we display the diffusion encoding modules of the (a) diffusion-weighted spin-echo (DW-SE) and (b) diffusion-weighted steady-state free precession (DW-SSFP) sequence. DW-SSFP consists of a single RF pulse and diffusion gradient per TR (typically 20 – 40 ms). Magnetisation accumulates diffusion contrast over several TRs, consistent with dephasing and rephasing of magnetisation due to gradient pairs in the DW-SE. The resulting steady-state can be considered a superposition of multiple magnetisation components with different histories – e.g., pairs of diffusion-weighted gradients separated by a variable integer number of TRs that lead to different degrees of diffusion weighting. This creates a composite signal corresponding to a summation of these components, with non-trivial signal attenuation.

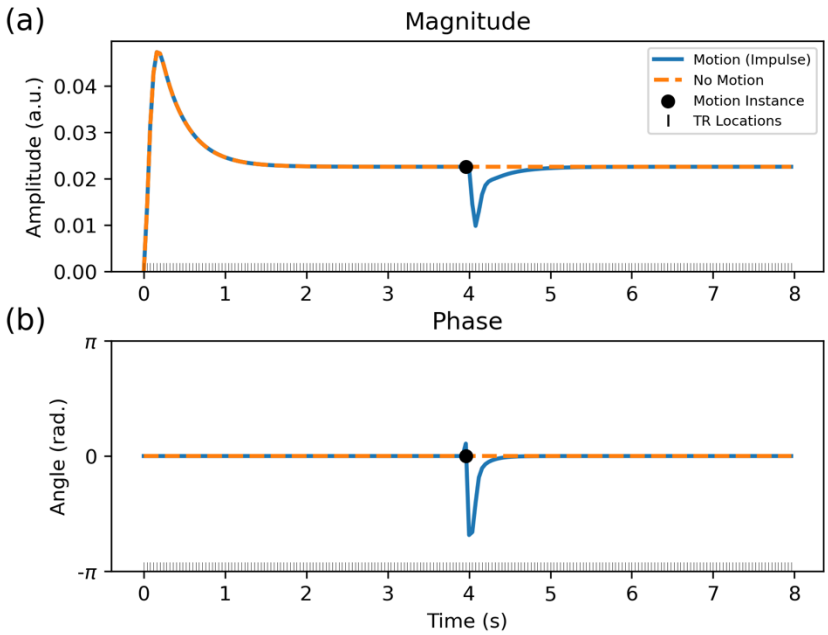

Figure 2: **DW-SSFP signal evolution with instantaneous motion.** Here we display a simulated 1D time-series profile of the DW-SSFP (a) magnitude and (b) phase signal over 200 TRs. After ~50 TRs (2 s), the signal reaches a steady state. A single instance of motion during one TR (black dot) perturbs the steady state. This motion-corrupted magnetisation persists and contributes to future TRs, leading to a slow recovery to the original steady state, with both the magnitude and phase signal impacted. Sequence parameters based on the experimental investigation performed in Miller & Pauly[18], setting $G = 40\ \mathrm{mT/m}$, $\delta = 6.5\ \mathrm{ms}$, $\alpha = 30^{o}$, $\mathrm{TR} = 40\ \mathrm{ms}$ and $\phi = 0^{o}$. The impulse motion was modelled using a velocity of 1.5 mm/s using the proposed EPG-motion framework (see Theory). Sample parameters based on approximate in vivo values in brain tissue at 3T[34], defining $D = 1 \cdot 10^{-3}\ \mathrm{mm^2/s}$, $T_1 = 832\ \mathrm{ms}$ and $T_2 = 110\ \mathrm{ms}$.

There are several ways to interpret the corruption of signal phase and magnitude in DW-SSFP. One approach to consider is that as DW-SSFP is a steady-state sequence, magnetisation excited in a single TR persists and evolves over multiple TRs. Over time the DW-SSFP signal reaches a steady-state (Figure 2), with the signal reflecting a weighted sum of magnetisation components with different evolution histories. Motion at any timepoint leads to phase corruption of the excited magnetisation, which over future TRs will combine with magnetisation components with different motion histories and associated phase corruption, leading to phase cancellation and subsequent magnitude loss (Figure 2). This includes the combination of phase corrupted magnetisation with 'fresh' magnetisation (i.e. longitudinally recovered magnetisation that has been excited into the transverse plane) that has no motion history. This form of magnitude loss is independent of the readout scheme and k-space FOV, and motion-induced magnitude loss can exist even if no motion is present during a given TR (as indicated by the slow signal recovery after an instantaneous motion in Figure 2).

From the perspective of Extended Phase Graphs[35] (EPG), magnitude corruption of the DW-SSFP signal can be interpreted as a weighted sum of signal-forming magnetisation pathways with different phase values. More generally, the loss of signal magnitude in DW-SSFP is dependent on the properties of the diffusion-encoding scheme, the diffusion gradient orientation, and the evolution of the motion profile over time (see Theory), meaning magnitude changes do not simply lead to a global loss of SNR, and must be corrected for accurate diffusion modelling.

Several methods have been proposed to address motion artefacts in DW-SSFP[17–21], generally by adopting navigator-based phase corrections that were originally proposed for DW-SE. A key limitation of these previous methods is that they do not account for the loss of signal magnitude arising from the combination of magnetisation components with different evolution histories, leading to residual artefacts in reconstructed images. One notable exception is work by O'Halloran et al.[22] establishing a prospective motion-correction method for DW-SSFP utilising real-time information to estimate and correct for deviations in image phase arising from rigid-body motion of the subject, providing partial attenuation of magnitude signal loss.

In this work, we perform a theoretical investigation, and experimental validation, into the impact of subject motion on with the DW-SSFP signal associated with the underlying magnetisation distribution (i.e. independent of the readout and k-space FOV). We demonstrate that the loss of motion-induced signal magnitude associated with the magnetisation distribution can be estimated and corrected *retrospectively* using timeseries data capturing the evolution of the DW-SSFP signal.

To achieve this, we first introduce a theoretical framework based on EPG[35] (building on a previous abstract[36]) to characterise how the DW-SSFP signal is corrupted by motion arising from (1) rigid-body translations, (2) rigid-body rotations, and (3) brain pulsatility associated with the cardiac cycle. We validate the proposed framework using Monte Carlo simulations, and use the framework to visualise how these different types of motion impact DW-SSFP images assuming an instantaneous (i.e. analogous to a single-shot) readout. We subsequently demonstrate that motion-corrupted DW-SSFP data contain sufficient information to estimate and reconstruct the motion-corrected signal, evaluating the framework experimentally using 2D low-resolution single-shot DW-SSFP timeseries data. Open-source code is provided to enable researchers to replicate many of the findings in this manuscript and perform their own investigations on the impact of subject motion on DW-SSFP data, available at github.com/BenjaminTendler/MotionCorrectionDWSSFP.

Theory

Extended Phase Graphs (EPG)

In this work, we use EPG to characterise the impact of motion on the DW-SSFP signal. Briefly, EPG describes a widely adopted framework for modelling the magnetisation evolution of an MRI sequence. It provides a solution to the Bloch equations[37], reparameterising magnetisation as a Fourier basis with distinct phase states of dephasing order k, defining:

- Longitudinal ($\tilde{Z}$) and transverse ($\tilde{F}$) magnetisation components with different k states ($\tilde{Z}_k$, $\tilde{F}_k$).
- RF pulses acting as an operator that mixes $\tilde{Z}_k$ and $\tilde{F}_k$ components.
- Magnetic field gradients acting on $\tilde{F}_k$ components by increasing their dephasing order.

EPG describes the magnetisation evolution in each TR as a series of steps. An RF pulse operator first mixes $\tilde{Z}_k$ and $\tilde{F}_k$ components, followed by the application of additional operators (describing relaxation, motion, diffusion etc) during the TR, with the dephasing order (k) of magnetisation components updated based on the applied magnetic field gradients. Mathematically, the EPG framework formalises magnetisation components as 3x1 vectors of $\tilde{F}_k$ and $\tilde{Z}_k$ states, acted on by 3x3 operator matrices. For readers unfamiliar with EPG signal representations, we recommend the review article by Weigel[35].

Extended Phase Graphs and diffusion

The impact of diffusion attenuation has been previously incorporated into an EPG framework via a diffusion operator[38], $\mathbf{D}$. For a periodic sequence, in which each TR contains a diffusion gradient of duration δ, $\mathbf{D}$ is given by:

$$\mathbf{D} = \begin{bmatrix} e^{-\left(\left(k_1+\frac{\Delta k}{2}\right)^2+\frac{\Delta k^2}{12}\right)\cdot\delta\cdot \mathrm{D}} \cdot e^{-k_2^2\cdot(\mathrm{TR}-\delta)\cdot \mathrm{D}} & 0 & 0 \\ 0 & e^{-\left(\left(k_1+\frac{\Delta k}{2}\right)^2+\frac{\Delta k^2}{12}\right)\cdot\delta\cdot \mathrm{D}} \cdot e^{-k_2^2\cdot(\mathrm{TR}-\delta)\cdot \mathrm{D}} & 0 \\ 0 & 0 & e^{-k_1^2\cdot \mathrm{TR}\cdot \mathrm{D}} \end{bmatrix}, \quad [1]$$

where $k_1$and k_2 are the dephasing order before and after application of the diffusion gradient, $\Delta k = k_2 - k_1$, and D is the diffusion coefficient. When considering diffusion gradients, we can define the dephasing order as an integer multiple of the diffusion gradient's q-value, $q = \int \gamma \cdot G(t) \cdot dt$, with the change in dephasing order during the application of a diffusion gradient equivalent to $\Delta k = q$.

The product of the two exponentials at locations $\mathbf{D}_{1,1}$ and $\mathbf{D}_{2,2}$ characterises the diffusion attenuation associated with transverse magnetisation during (1) the application of a diffusion gradient of duration δ and (2) the

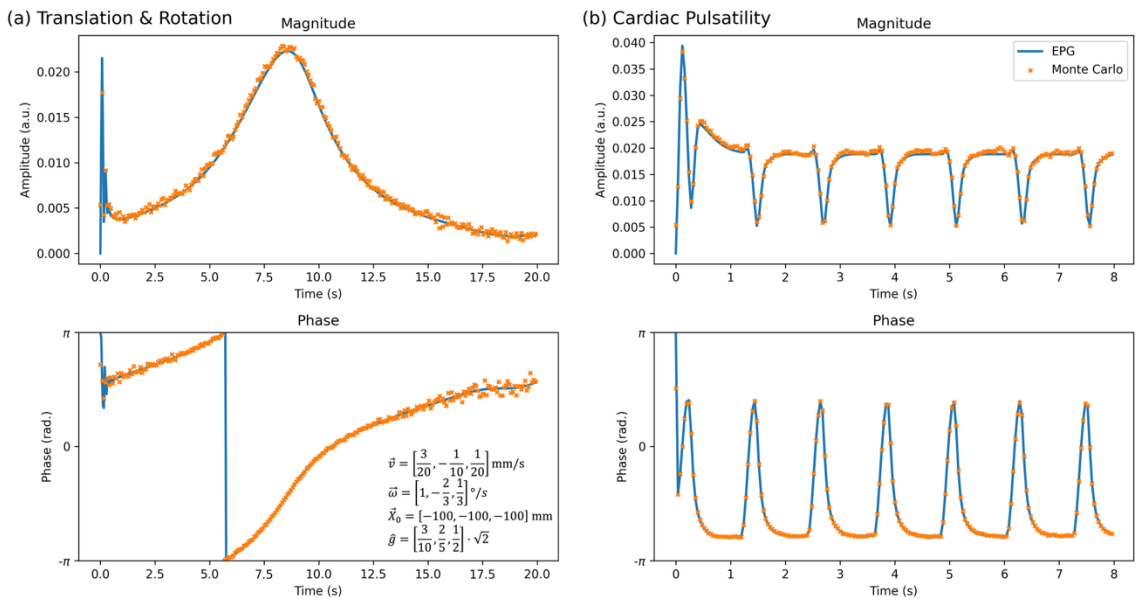

Figure 3: **Comparing the EPG-motion operator with Monte Carlo simulations**. Motion-corrupted DW-SSFP time-series data simulated using the proposed EPG-motion operator and Monte Carlo simulations for (a) fixed rigid body translation/rotation across all three dimensions and (b) cardiac pulsatility. The two approaches give excellent agreement across the time-course of the investigation. Rigid body motion parameters associated with Eqs. [3-5] are displayed in (a), where $\vec{X}_0$ defines the initial voxel location relative to the centre of rotation. Pulsatility velocity profile (Supporting Information Figure S1) based visually on Greitz et al.[39], simulated defining the maximum pulsatility velocity $\vec{v}_{\mathrm{Card}} = [0, 0, 0.4]$ mm/s and $\hat{g} = [0,0,1]$. Yellow dots correspond to the Monte-Carlo signal estimates at the end of each TR, with simulations performed using 100 timesteps per TR. Sequence parameters based on the experimental investigation performed in Miller & Pauly[18], setting $\mathrm{G} = 40$ mT/m, $\delta = 6.5$ ms, $\alpha = 30^{\mathrm{o}}$, TR $= 40$ ms and $\phi = 0^{\mathrm{o}}$. Sample parameters were based on approximate in vivo values in brain tissue at 3T[34], defining $\mathrm{D} = 1 \cdot 10^{-3}$ mm^2/s, $\mathrm{T}_1 = 832$ ms and $\mathrm{T}_2 = 110$ ms. See Methods for an overview of the Monte Carlo implementation.

remaining TR period. The exponential at location $\mathbf{D}_{3,3}$ characterises the diffusion attenuation experienced by longitudinal magnetisation in a single TR.

Extended Phase Graphs and motion

Analogous to the description of the diffusion operator in the previous section, we can characterise motion in EPG via a motion operator, $\mathbf{J}$. In this work, we extend previous descriptions of $\mathbf{J}$[35] to incorporate (1) gradients of fixed duration, (2) subject rotation, and (3) time-dependence. Assuming motion as linear (i.e. constant translational/rotational velocity), we can define:

$$\mathbf{J} = \begin{bmatrix} e^{-i\cdot\frac{k_1+k_2}{2}\cdot\delta\cdot V} \cdot e^{-i\cdot k_2\cdot(\mathrm{TR}-\delta)\cdot V} & 0 & 0 \\ 0 & e^{i\cdot\frac{k_1+k_2}{2}\cdot\delta\cdot V} \cdot e^{i\cdot k_2\cdot(\mathrm{TR}-\delta)\cdot V} & 0 \\ 0 & 0 & e^{-i\cdot k_1\cdot\mathrm{TR}\cdot V} \end{bmatrix}, \qquad [2]$$

where:

$$V = \vec{v}\cdot\hat{g} + (\hat{g}\times\vec{\omega})\cdot\vec{X}, \qquad [3]$$

$\hat{g}$ = unit vector describing gradient orientation, $\vec{v}$ = translational velocity, $\vec{\omega}$ = rotational velocity and $\vec{X}$ = spatial location (relative to the centre of rotation). To incorporate changes in the motion profile across TRs, we can define:

$$V_{\mathrm{n}} = \vec{v}_{\mathrm{n}}\cdot\hat{g} + (\hat{g}\times\vec{\omega}_{\mathrm{n}})\cdot\vec{X}_{\mathrm{n}}, \qquad [4]$$

where the subscript indicates the parameters for the nth TR, and V_{n} is a scalar constant representing the component of instantaneous velocity along the orientation of the diffusion gradient during a given TR. We subsequently refer to the evolution of V_{n} across multiple TRs as $V(t)$.

The steady-state diffusion signal persists for several seconds over multiple TRs, with the signal lifetime dictated primarily by T_1. When considering forms of motion that are dependent on the spatial location $\vec{X}$, the motion operator must account for cumulative changes in $\vec{X}$ over the time-course of an acquisition. Assuming a single time-step per TR, we define:

$$\vec{X}_{\mathrm{n+1}} = \boldsymbol{R}(\vec{\theta}_{\mathrm{n}})\vec{X}_{\mathrm{n}} + \vec{x}_{\mathrm{n}}, \qquad [5]$$

where $\boldsymbol{R}(\vec{\theta})$ is a 3D rotation matrix operation = $\boldsymbol{R_z}(\theta_z)\boldsymbol{R_y}(\theta_y)\boldsymbol{R_x}(\theta_x)$, $\vec{\theta}_{\mathrm{n}} = \vec{\omega}_{\mathrm{n}} \cdot \mathrm{TR}$ and $\vec{x}_{\mathrm{n}} = \vec{v}_{\mathrm{n}} \cdot \mathrm{TR}$. We note that the proposed motion operator is not specific to DW-SSFP, and could be incorporated into EPG schemes investigating the impact of motion on arbitrary MRI sequences.

Figure 3 compares a simulated time-series evolution of the DW-SSFP signal using (1) EPG integrating the proposed motion operator and (2) Monte Carlo simulations for fixed rigid-body motion (left column) and a temporally varying motion profile characterising cardiac pulsatility (right column). Excellent agreement is found between the two simulation approaches. Notably, motion in the EPG implementation was modelled using a single timestep per TR (Eq. [4]), with motion in the Monte Carlo implementation modelled using 100 timesteps per TR. Agreement between the two approaches suggests that the short TR of DW-SSFP enables motion to be captured as a single parameter in each TR. Full details of the Monte Carlo implementation are provided in the Methods.

Motion induced image corruption in DW-SSFP

To visualise the impact of motion on DW-SSFP images, we can utilise the proposed EPG-motion framework to simulate the signal evolution of individual voxels in a DW-SSFP dataset. Figure 4a-d displays synthetised DW-SSFP images assuming an instantaneous readout (i.e. analogous to a single-shot readout) incorporating (a) no motion, (b) translation along a single dimension, (c) rotation along a single dimension and (d) cardiac pulsatility. Here we observe that even simple forms of rigid-body motion lead to complicated spatial changes in both signal magnitude and phase. Signal changes arising from pulsatile motion (Figure 4d) give good visual agreement to loss of signal magnitude observed previously[18,21], with artefacts propagating into images synthesised simulating a segmented readout (i.e. a subset of k-space is sampled per TR at different periods of the cardiac cycle, and combined to form the final image) (Figure 4e). Comparisons with DW-SE images acquired with the same motion properties and an instantaneous readout are displayed in Supporting Information Figure S3, where only changes in the spatial phase profile are observed.

In addition to the loss of signal magnitude in motion-corrupted DW-SSFP data, resulting phase images display local tissue-type contrast (e.g. delineation of CSF filled regions) that are not observed in motion-corrupted DW-SE data (i.e the flat phase maps in Supporting Information Figure S3). This local contrast reflects the interplay between motion and the local diffusion coefficient. Specifically, when considering EPG, an increased diffusion coefficient rapidly attenuates the relative contribution of signal forming pathways associated with strong diffusion-weighting, analogous to reducing the relative contribution of signal forming pathways associated with greater motion-corruption (Supporting Information Figure S4). The local diffusion coefficient, D, must therefore be estimated as part of the motion-reconstruction procedure.

The DW-SSFP signal has known dependencies on local tissue relaxation properties (T_1 & T_2) and B_1[40], which must also be estimated (via complementary mapping techniques) for accurate diffusion and motion modelling. From the perspective of EPG, this property arises as T_1, T_2, and B_1 values additionally modulate the relative contribution of different DW-SSFP signal-forming magnetisation pathways and interact with their relative motion sensitivity, analogous to the description of diffusion coefficients in the previous paragraph. T_1, T_2 and B_1 mapping procedures using complementary imaging sequences have formed a routine part of many DW-SSFP studies estimating quantitative diffusion parameters, with a similar approach used in this study (see Methods).

Does the DW-SSFP signal contain sufficient information to reconstruct motion-free estimates?

Earlier in this manuscript, we proposed an EPG operator for motion characterisation (Eq. [2]), validated using Monte Carlo simulations (Figure 3). Eqs. [2-4] describe motion in DW-SSFP as fully characterised provided one has knowledge of evolution of V_{n} across TRs, $V(t)$ (Eq. [4]). Importantly, whilst individual EPG pathways are

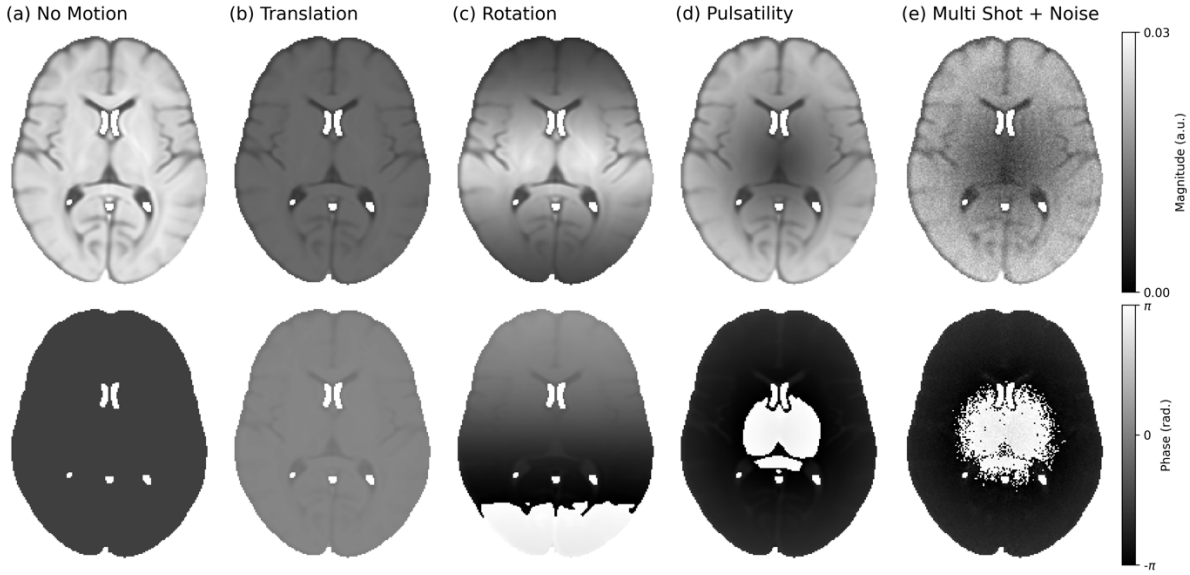

Figure 4: **Impact of motion on DW-SSFP images**. (a-d) displays simulated DW-SSFP images incorporating (a) no motion (b) constant translation ($\vec{v} = [0,0,0.2]$ mm/s), (c) constant rotation ($\vec{\omega} = [0.2,0,0]$ ^{o}/s) and (d) cardiac pulsatility, simulated with an instantaneous readout. (e) displays a simulated DW-SSFP image acquired with a segmented readout (three-line cartesian readout per TR) incorporating cardiac pulsatility only with added Gaussian noise ($\mathrm{SNR} \sim 20$), where each readout is associated with a different component of the cardiac cycle. Images synthesised using the HCP1065 DTI template mean diffusivity map, available as part of FSL[41]. Pulsatility timeseries profile and relative velocity map based visually on Greitz et al.[39], provided in Supporting Information Figures S1 and S2, here setting the maximum pulsatility velocity $\vec{v}_{\mathrm{Card}} = [0, 0, 0.4]$ mm/s and $\hat{g} = [0,0,1]$. Sequence parameters based on the experimental investigation performed in Miller & Pauly[18], setting $\mathrm{G} = 40$ mT/m, $\delta = 6.5$ ms, $\alpha = 30^{o}$, TR $= 40$ ms, $\phi = 0^{o}$. Relaxation parameters (set equal across all voxels) were based on approximate in vivo values in brain tissue at 3T[34], setting $\mathrm{T}_1 = 832$ ms and $\mathrm{T}_2 = 110$ ms. Images (a-d) are displayed for the 150th TR, corresponding to a simulation duration of 6 seconds. (e) was synthesised using data from the 101st to the 188th TR (ignoring systole), corresponding to an acquisition duration of 3.48 s. Voxels were modelled as independent (i.e. the voxel location is stationary over the time-course of the simulation).

associated with different levels of motion corruption in each TR, this difference solely arises from the interplay of $V(t)$ with a pathway's *known* dephasing order, k. This raises the question of whether DW-SSFP data can contain sufficient information to simultaneously estimate $V(t)$ as part of the signal characterisation to reconstruct motion-corrected images. The remainder of the manuscript investigates this using both synthetic and experimental data.

Methods

EPG-motion Framework

Software for simulating (1) the time-series motion operator, $V(t)$, and (2) the DW-SSFP signal incorporating the impact of subject motion (see Theory) was implemented in Python (3.13.2). The provided software allows the modelling of voxelwise and imaging timeseries DW-SSFP data based on a user-defined set of sequence parameters ($G, \tau, TR, \theta, \phi$), sample properties ($T_1, T_2, D, B_1$), and motion operators (translational, rotational and pulsatile). When simulating 2D and 3D images (e.g. Figure 4), the software models each voxel as independent (i.e. the voxel location is stationary over the time-course of the simulation).

The software was built using NumPy (2.2.4), accelerated with the Numba compiler (0.61.2). For reference, the time required to synthesise an arbitrary $V(\mathrm{t})$ profile and subsequent motion corrupted DW-SSFP signal over 200 TRs is ~ 5 ms (single voxel), ~ 10 s (2D slice) and ~ 10 m (3D volume) on a personal laptop.

The software is open source, and available at https://github.com/BenjaminTendler/MotionCorrectionDWSSFP. This includes demos to perform (1) forward simulations and (2) parameter estimation from time-series voxelwise/imaging DW-SSFP data, alongside scripts to recreate many of the figures in this manuscript.

Monte Carlo Simulations

To validate the proposed EPG-motion framework, 1D DW-SSFP time-series magnitude and phase signals incorporating rigid body (translational and rotational) motion and cardiac pulsatility were synthesised using Monte Carlo simulations (Figure 3). Briefly, isochromat trajectories were generated using the Camino *datasynth* function[42], modified to produce trajectories that followed a Gaussian distribution of displacements per timestep (10^5 spins, 100 timesteps per TR). To simulate motion, the location of individual isochromats was updated per timestep via translational and/or rotational (via a rotation matrix) operations using custom software. For the pulsatility simulations, the continuous time-series velocity profile (Supporting Information Figure S1) was averaged across the window associated with each timestep and discretised to define the isochromat displacement per timestep.

For the Monte Carlo simulations, the DW-SSFP signal was modelled using a custom Bloch equation simulator, implemented in MATLAB (2023a, The MathWorks, Inc., Natick, MA). Sequence parameters were based on the experimental investigation performed in Miller & Pauly[18] ($G = 40\ \mathrm{mT/m}$, $\delta = 6.5\ \mathrm{ms}$, $\alpha = 30^{\mathrm{o}}$, TR $= 40\ \mathrm{ms}$ and RF phase $\phi = 0^{\mathrm{o}}$), with sample parameters based on approximate in vivo values in brain tissue at 3T[34], defining $\mathrm{D} = 1 \cdot 10^{-3}\ \mathrm{mm^2/s}$, $\mathrm{T_1} = 832\ \mathrm{ms}$ and $\mathrm{T_2} = 110\ \mathrm{ms}$.

Monte Carlo simulations incorporating translational and rotational motion were synthesised defining translational velocity, $\vec{v} = \left[\frac{3}{20}, -\frac{1}{10}, \frac{1}{20}\right] \mathrm{mm/s}$, rotational velocity, $\vec{\omega} = \left[1, -\frac{2}{3}, \frac{1}{3}\right] {}^{\circ}/s$, initial spatial position, $\vec{X}_0 = [-100, -100, -100]\ \mathrm{mm}$, and diffusion gradient orientation, $\hat{g} = \left[\frac{3}{10}, \frac{2}{5}, \frac{1}{2}\right] \cdot \sqrt{2}$ (see Eq. [3] and surrounding text for definitions). These parameters were chosen to characterise an arbitrary, constant rigid body motion across all three spatial dimensions, achieving large changes in signal magnitude and phase. The pulsatility velocity profile (characterising time-dependent motion) is visualised in Supporting Information Figure S1, setting the maximum pulsatility velocity $\vec{v}_{\mathrm{Card}} = [0, 0, 0.4]\ \mathrm{mm/s}$ and $\hat{g} = [0,0,1]$.

Parameter Estimation from Simulated DW-SSFP Data (Monte Carlo)

Using the proposed EPG-motion framework, the diffusion coefficient (D), phase offset (ϕ), and $V(\mathrm{t})$ profile were estimated from 1D DW-SSFP timeseries data arising from the Monte Carlo simulations incorporating pulsatility (Figure 3b). The phase offset (ϕ) reflects deviations in the true phase offset versus the defined RF phase angle, equivalent in simulations ($\phi = 0^{\mathrm{o}}$) but differing experimentally (arising from spatial B_0 and B_1 profiles). To more accurately reflect experimental conditions, Gaussian noise was added to the simulated signal, leading to a final SNR of 20. The fitting procedure was implemented in Python (3.13.2) using the Trust Region Reflective algorithm provided by SciPy *curve_fit* (1.15.2). Specifically, the EPG-motion framework was incorporated as a forward model, with the parameter estimation procedure identifying parameters that minimised the cost function with the motion-corrupted Monte-Carlo DW-SSFP signal. To accelerate the fitting procedure, an analytical Jacobian function was derived for all parameters (except for the derivative with respect to D, which was estimated numerically).

The simulated DW-SSFP timeseries data consisted of 200 TRs. Parameter estimation was performed using a time window of 100 TRs of steady-state signal (after 100 TRs, from 3.96 s in Figure 3b). A single motion parameter was estimated per TR, corresponding to 102 parameters in total (D + ϕ + $V(\mathrm{t})$). To facilitate estimation of $V(\mathrm{t})$, the parameter estimation region was split into two components corresponding to (1) dummy measurements (first 25 TRs) and (2) measured signal (remaining 75 TRs). The dummy measurements reflect a series of TRs which were not incorporated into the cost function evaluation. This is important as motion effects build up over several TRs in DW-SSFP (Figure 2). Specifically, the dummy region makes it possible to accurately characterise the motion-corrupted signal from the first TR of the measured signal region by allowing the signal to reach a steady-state incorporating the effects of motion prior to this timepoint. Ten repeats were performed with different noise instances to characterise the robustness of the fitting approach. The fitting procedure averaged at ~4 seconds per noise instance on a personal laptop (Macbook Pro, Sonoma 14.5, M1, 16GB RAM).

To understand the impact of incorporating motion into the parameter estimation procedure, an identical fitting approach was implemented without estimation of the $V(\mathrm{t})$ operator (i.e. conventional EPG). This corresponds to the estimation of two parameters per simulation (D + ϕ).

Estimation of D as a Function of SNR and Pulsatile Velocity

To assess the robustness of characterising D from motion-corrupted DW-SSFP timeseries data, simulations were performed incorporating pulsatile motion for a range of SNR levels (10, 20, 50, + no noise) and maximum pulsatility velocities (0 to 1.5 mm/s in 0.3 mm/s increments), where 0 mm/s corresponds to a no motion case and 1.5 mm/s corresponds to a previous experimental estimate of maximum pulsatile velocity in brain tissue[39]. Ten repeats were performed per SNR level and velocity instance, corresponding to 240 simulations in total. Simulations with maximum pulsatile velocity = 0 mm/s are equivalent to implementing the EPG-motion framework when no motion is present.

Experimental Data Acquisition

2D time-series DW-SSFP data were acquired in a single axial slice of the brain (single subject) on a 3T Siemens Prisma scanner (32 channel head coil). The subject gave informed consent with data acquisition in accordance with local ethics committees. Sequence parameters were optimised for a target effective b-value, $\mathrm{b_{eff}} = 500\ \mathrm{s/mm^2}$, setting $G = 26.7$ and $63.6\ \mathrm{mT/m}$, $\delta = 3.08\ \mathrm{ms}$, $\mathrm{TR} = 26\ \mathrm{ms}$, $\alpha = 31°$, $\phi = 0°$, $\mathrm{TE} = 15\ \mathrm{ms}$, $\mathrm{BW} = 2405\ \mathrm{Hz/Pix}$, resolution = $6 \times 6 \times 6\ \mathrm{mm^3}$, matrix size 32×32. b_0-equivalent data were also acquired with $G = 26.7\ \mathrm{mT/m}$, producing images that achieve the DW-SSFP spoiling condition with very low diffusion weighting ($\mathrm{b_{eff}} = 100\ \mathrm{s/mm^2}$), henceforth referred to as b_0.

To ensure the signal reached a steady-state, dummy measurements were performed for 5 seconds prior to data acquisition. Sequence parameters were chosen via an optimisation routine that maximised SNR-efficiency for the target effective b-value[8,43]. To evaluate the relationship between the DW-SSFP timeseries data and cardiac pulsatility, Pulse oximeter recordings were simultaneously acquired over the time course of the acquisition.

The time-series data consisted of 384 consecutive measurements in a single axial slice of the brain, corresponding to 10 seconds of data. A fully sampled image was acquired in each TR (i.e. equivalent to a 'single-shot' readout) to characterise the temporal dynamics of the DW-SSFP signal independent of a segmented readout scheme. 12 diffusion directions were acquired in total, with both b_0 & diffusion-weighted volumes acquired per direction. The raw data (*.dat*) was exported from the scanner and reconstructed using *mapVBVD*[44]., with coil-combination performed using SVD and ESPIRiT[45,46]

The DW-SSFP signal has known dependencies on tissue relaxation (T_1 and T_2) properties and the B_1 profile. To improve the accuracy of modelling, complementary T_1, T_2 and B_1 maps were estimated in the same subject using a spin echo EPI with inversion preparation (ep2d_se, one sequence per inversion time), multi-echo spin-echo (se_mc) and 3DREAM[47] sequence. Full details of the sequence parameters and processing are provided in Supporting Information Table S1.

To facilitate comparisons, 2D DW-SE data was additionally acquired within the same subject, closely matching the acquisition scheme of the DW-SSFP data ($\mathrm{b_0}$ and $500\ \mathrm{s/mm^2}$, 12 diffusion directions). Full details of the DW-SE sequence parameters and image processing are provided in Supporting Information Table S1.

Parameter Estimation from Experimental DW-SSFP Data

The diffusion coefficient (D), signal amplitude (S_0), phase offset (ϕ), and $V(\mathrm{t})$ operator were estimated from experimental DW-SSFP timeseries data using the proposed EPG-motion framework. The fitting procedure was implemented in Python (3.13.2) as described above, fitting simultaneously to the time-series $\mathrm{b_0}$ and $500\ \mathrm{s/mm^2}$ data. Fitting was performed independently for each voxel and diffusion direction, estimating a single diffusion coefficient per voxel.

For the fitting procedure, DW-SSFP timeseries data was simulated for 509 TRs. This consisted of 100 TRs to ensure the simulated signal reached a steady-state, 25 TRs dummy measurements, and 384 TRs where comparisons were made to the acquired experimental data. A single motion parameter was estimated per TR, corresponding to the estimation of 822 parameters per voxel ($D + S_0 + \phi_{b0} + \phi_{b500} + T_{b0}(\mathrm{t}) + T_{b500}(\mathrm{t})$). Parameter estimation was on the time order of ~30 seconds per voxel on a personal laptop (Macbook Pro,

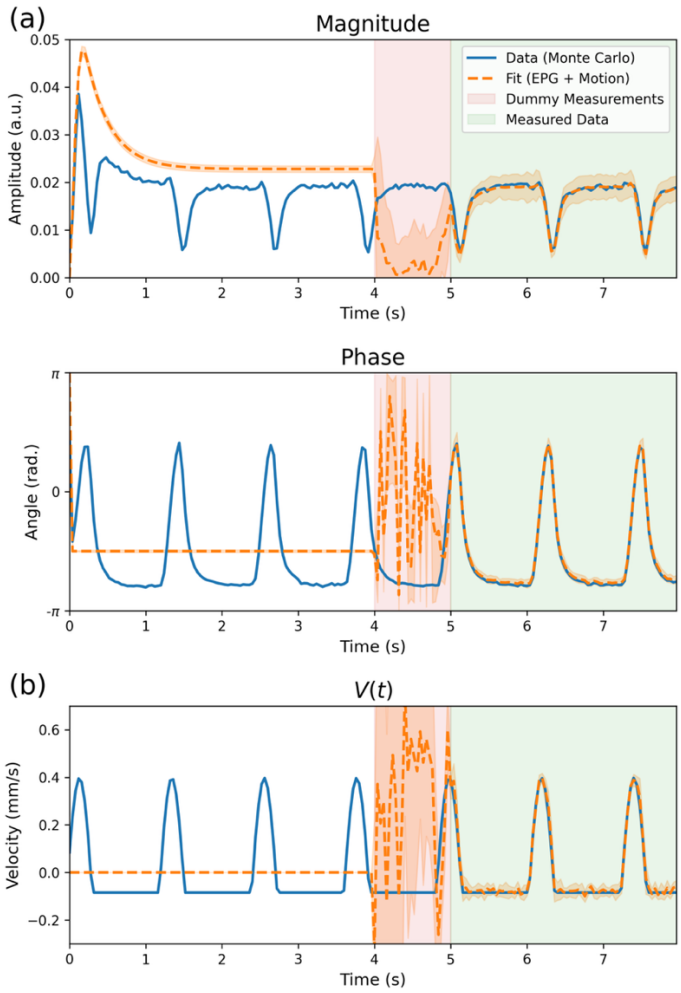

Figure 5: **Estimation of $V(t)$ from simulated DW-SSFP time-series data.** (a) displays DW-SSFP time-series magnitude and phase data (blue) incorporating cardiac pulsatility + Gaussian noise ($\mathrm{SNR} = 20$) synthesised using Monte Carlo simulations. Fitting to the Monte Carlo data via the proposed EPG-Motion framework accurately characterises the DW-SSFP time-series profile (orange) in the measured data region (green box). (b) The estimated time-series profile of $V(t)$ (reflecting the component of instantaneous velocity in the direction of the diffusion gradient across TRs) closely matches the ground truth in the measured data region (green), reflecting the possibility of characterising motion solely from the DW-SSFP signal. The dummy measurements (pink box) reflect a series of TRs where no comparison to the simulated data was performed. This is important as motion effects build up over several TRs in DW-SSFP (Figure 2), facilitating precise estimation of the DW-SSFP signal in the first TR of the measured data region. The white box reflects a series of TRs where the simulation reached a steady state. Here the dashed orange line represents the average estimate over the 10 noise repeats, with the orange shaded region surrounding the fitted line corresponding to the standard deviation over the 10 noise repeats.

Sonoma 14.5, M1, 16GB RAM). Finally, a tensor was reconstructed from the estimated D maps acquired across all 12 orientations using custom software.

To understand the impact of incorporating motion into the parameter estimation procedure, an identical fitting approach was implemented without estimation of the $V(\mathrm{t})$ operator (i.e. conventional EPG). This corresponded to the estimation of four parameters per simulation (D + S_0 + ϕ_{b0} + ϕ_{b500}).

Results

Figure 5 displays the estimated DW-SSFP time-series and $V(\mathrm{t})$ operator using the proposed EPG-motion framework, arising from Monte Carlo simulations of the steady-state DW-SSFP signal incorporating pulsatile motion with added Gaussian noise. Excellent agreement is found over the fitted data region (green box), indicating that simultaneous estimation of $V(t)$ and D is possible from DW-SSFP timeseries data.

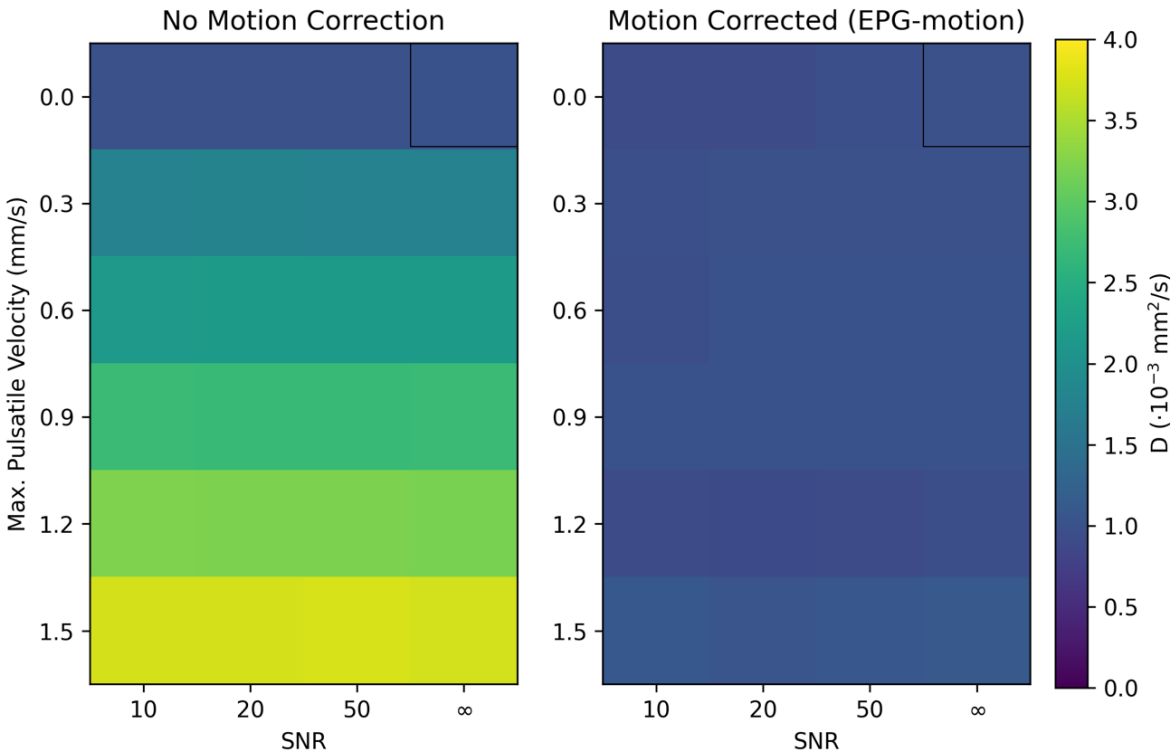

Figure 6: **Characterisation of D as a function of SNR and maximum pulsatile velocity amplitude.** (a) and (b) display the estimated diffusion coefficient, D, derived from DW-SSFP timeseries data as a function of SNR (x-axis) and maximum pulsatile velocity (y-axis). The two plots correspond to parameter estimation assuming (a) no motion correction and (b) motion correction using the proposed EPG-motion framework. The black box in the top right corresponds to the ground truth estimate (no motion, SNR = ∞). No incorporation of motion in parameter estimation (a) led to a maximum bias of 275% in the estimation of D across the investigated velocity/SNR regime, increasing as a function of the maximum pulsatile velocity. Simultaneous estimation of motion parameters (b) led to a maximum bias of 12%. Figure displays the average D calculated from 10 simulated DW-SSFP timeseries repeats per SNR/velocity level.

When considering diffusion MRI acquisitions, the key parameter we want to accurately characterise is the diffusion coefficient, D. By means of comparison, given the simulated coefficient ($\mathrm{D} = 1 \cdot 10^{-3}\ \mathrm{mm}^2/\mathrm{s}$), fitting to the simulated data with no estimation of $V(t)$ (i.e. conventional EPG) yielded $\mathrm{D} = (2.00 \pm 0.02) \cdot 10^{-3}\ \mathrm{mm}^2/\mathrm{s}$. Fitting with the proposed EPG-motion framework estimated $\mathrm{D} = (0.99 \pm 0.04) \cdot 10^{-3}\ \mathrm{mm}^2/\mathrm{s}$.

Figure 6 displays the estimated diffusion coefficient from simulated pulsatile motion with varying SNR levels and maximum pulsatility velocity. Here we identify that the incorporation of motion properties in parameter estimation substantially reduces the misestimation of D. Specifically, no characterisation of subject motion (Figure 6a) led to biases in D of up to 275% across the investigated velocity/SNR regime, increasing as a function of the maximum pulsatile velocity. An equivalent investigation incorporating the estimation of motion parameters using the EPG-motion framework (Figure 6b) led to a maximum bias of 12%.

The motion-free simulations (Figure 6 – top row) with no added noise (Figure 6 – black box) estimated $0.998 \cdot 10^{-3}\ \mathrm{mm}^2/\mathrm{s}$ (with motion correction) and $1.000 \cdot 10^{-3}\ \mathrm{mm}^2/\mathrm{s}$ (no motion correction). A small bias was observed in the diffusion coefficient estimation at reduced SNR levels when incorporating motion correction (~8% at SNR = 10, Figure 6 - top left) for the motion-free simulations, which were not present in the parameter estimation procedure without motion correction (~0.4% at SNR = 10). This reflects an increased sensitivity of the proposed EPG-motion framework to data noise.

Figure 7 displays an example DW-SSFP timeseries and $V(t)$ profile estimated in a single voxel of experimental data acquired in the human brain. The timeseries corresponds to the voxel in the thalamus, with the diffusion gradient oriented along the anterior-posterior axis. The experimental timeseries data displays consistent

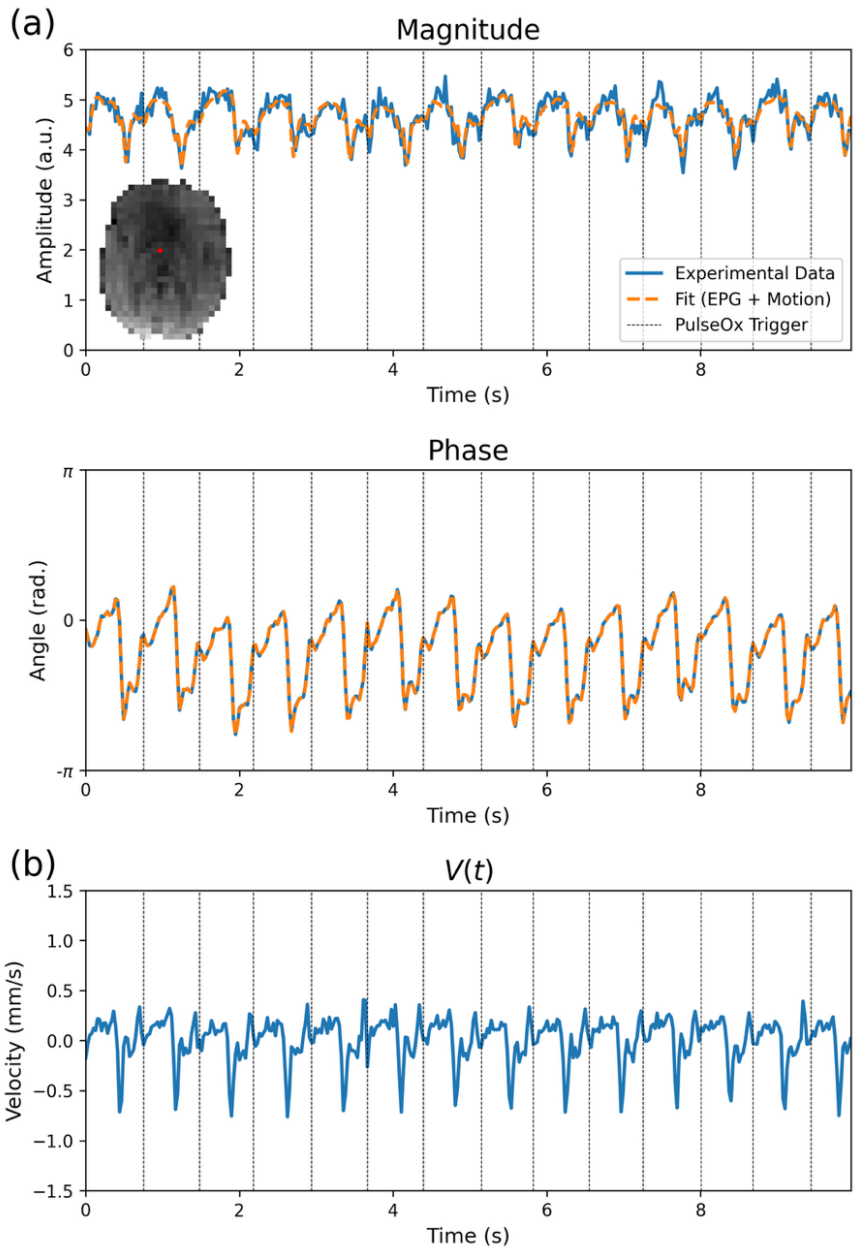

Figure 7: **DW-SSFP signal and $V(t)$ profile in a single voxel of experimental $\mathbf{b_{eff}} = \mathbf{500\ s/mm^2}$ data**. The experimental DW-SSFP signal profile (a) (blue lines) displays periodicity consistent with the timings of Pulse oximeter triggers (black vertical lines) acquired as part of the acquisition. Fitting to the experimental data using the proposed EPG-motion framework (orange line) gives excellent agreement to the experimental data, with the estimated velocity profile (b) displaying consistent periodic changes in tissue velocity, consistent with pulse oximeter trigger locations. Displayed timeseries corresponds to a single voxel in the thalamus (visualised in inset figure of experimental data in (a) – red voxel), with the diffusion gradient oriented along the anterior-posterior axis. $V(\mathrm{t})$ defined as the component of instantaneous velocity in the direction of the diffusion gradient across TRs (Eq. [4]).

characteristics to the DW-SSFP simulations incorporating cardiac pulsatility, with the periodicity of the DW-SSFP signal and $V(t)$ profile consistent with the recorded locations of pulse oximeter triggers.

Figure 8 displays the DW-SSFP timeseries magnitude data ($b_{\mathrm{eff}} = 500\ \mathrm{s/mm^2}$) across a portion of the cardiac cycle with the diffusion gradient oriented along the (a) right-left, (b) anterior-posterior and (c) foot-head direction. Subtle changes in signal amplitude are visible across the timeseries in (a) and (b), with considerable changes in signal amplitude along the foot-head direction (c). Here, even a modest b-value of $\mathrm{b_{eff}} = 500\ \mathrm{s/mm^2}$ leads to a substantial loss of signal along the foot-head direction in central regions of the brain.

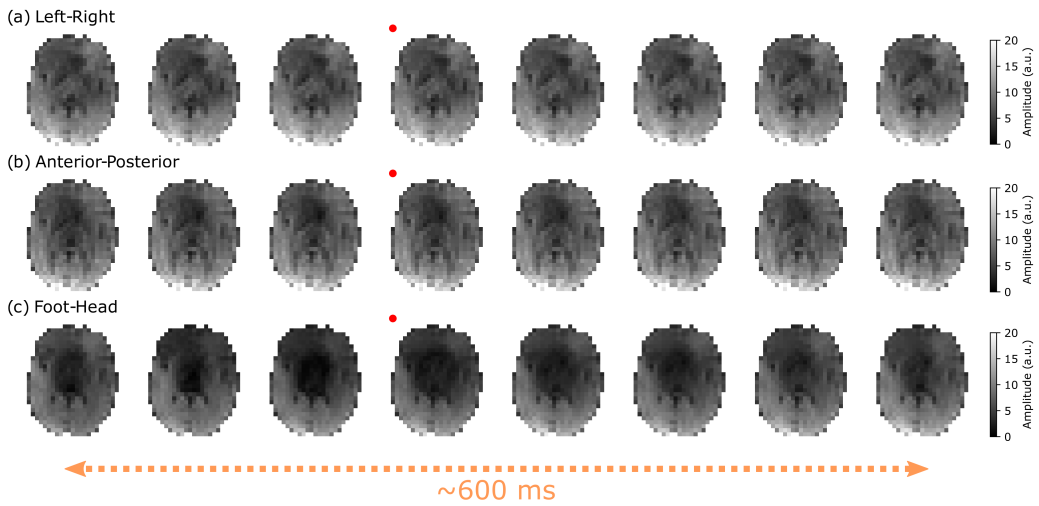

Figure 8: **Experimental DW-SSFP timeseries images.** (a-c) correspond to example $b_{\text{eff}} = 500\ \text{s/mm}^2$ data over time acquired with left-right (a), anterior posterior (b) and foot-head (c) gradient orientations. The change in signal is most prominent along the foot-head orientation, characterised by a substantial loss of signal in the central brain. Here the red dots indicate the image acquired at the timepoint of the pulse oximeter trigger, with the x-axis reflecting a subset of data acquired over 624 ms, with a gap of 78 ms between images (three TRs).

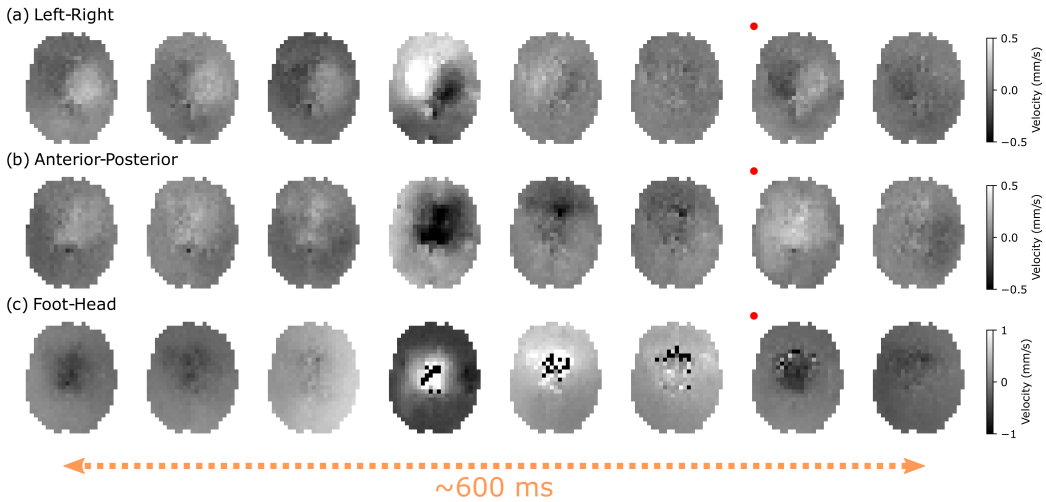

Figure 9: **Estimated $V(t)$ spatial maps.** (a-c) correspond to example $V(t)$ spatial maps estimated from the experimental DW-SSFP data acquired with $b_{\text{eff}} = 500\ \text{s/mm}^2$ along left-right (a), anterior-posterior (b) and foot-head (c) gradient orientations. Here the red dots indicate the image acquired at the timepoint of the pulse oximeter trigger (shifted by 260 ms versus Figure 8 to reflect time differences between the trigger and peak brain tissue velocity changes), with the x-axis reflecting a subset of data acquired over 624 ms, with a gap of 78 ms between images (three TRs). $V(\text{t})$ defined as the component of instantaneous velocity in the direction of the diffusion gradient across TRs (Eq. [4]).

Figure 9 displays the corresponding $V(t)$ maps estimated from the same portion of the cardiac cycle with the diffusion gradient oriented along the (a) left-right, (b) anterior-posterior and (c) foot-head direction. Here we observe smooth changes (both temporally and spatially) in $V(t)$. Importantly, each voxel in these images has been processed *independently*, with the arising spatial smoothness reflective of the consistency of velocity estimation across individual voxels. A notable exception arises from voxels in the centre of brain along the foot-head direction, where signal amplitudes are too low (Figure 8c) to reliably estimate motion parameters during peak systole (see Discussion).

The $V(t)$ maps display a consistent pattern of sharp velocity increases (associated with systole) followed by a slower velocity relaxation during diastole. The spatial patterns are consistent with previous investigations into brain pulsatility. Specifically, the asymmetric $V(t)$ profile associated with the left-right gradient orientation is

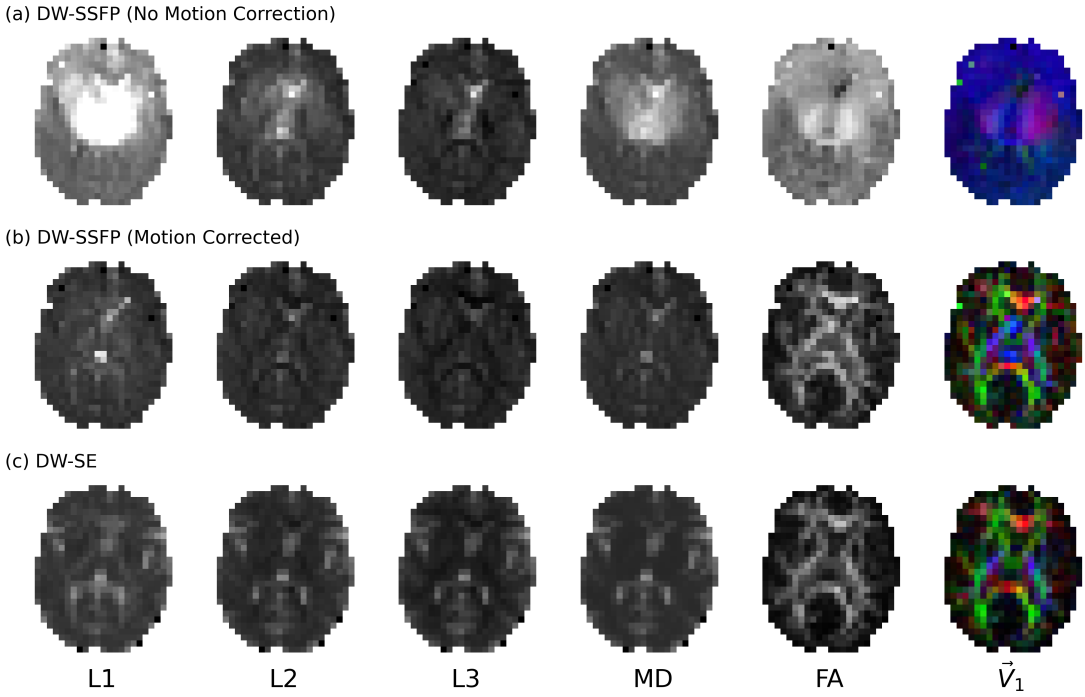

Figure 10: **Tensor Outputs.** Comparison of tensor outputs for (a) DW-SSFP data without motion correction, (b) DW-SSFP data with motion-correction (via the EPG-motion framework) and (c) comparison DW-SE data. Without motion-correction (a), DW-SSFP data display large spatial biases that obfuscate interpretation of tensor elements. Motion-corrected DW-SSFP data (b) display excellent visual agreement with complementary DW-SE estimates (c), eliminating spatial biases. Tensors reconstructed from individual diffusion coefficient maps estimated per orientation using custom code. Blue = Foot-Head, Red = Left-Right, Green = Anterior-Posterior.

consistent with previous observations by Adams et al.[48] and Terem et al.[49], with the $V(t)$ profile along the anterior-posterior axis consistent with observations in Greitz et al[39].

Finally, Figure 10 displays tensor estimates reconstructed from the 12 diffusion gradient orientations for (a) DW-SSFP timeseries data without motion correction, (b) DW-SSFP timeseries data with motion correction using the proposed EPG-motion framework, and (c) DW-SE data. Without performing motion correction, it is not possible to reconstruct informative spatial information in the tensor reconstruction. The observed artefacts arise as (i) diffusion coefficients along each orientation are incorrectly estimated due to the impact of subject motion on the DW-SSFP signal and (ii) the degree of misestimation is dependent on the diffusion gradient orientation. The 'blue-bias' observed on the uncorrected $\vec{V}_1$ maps is consistent with previous work acquiring in-vivo DW-SSFP data[21], arising from the greater motion sensitivity of data acquired with a foot-head diffusion gradient orientation.

Correction using the proposed EPG-motion framework leads to consistent tensor estimates across the whole image (Figure 10b), with excellent agreement to the complementary images reconstructed from DW-SE data (Figure 10c).

Discussion

EPG-motion Framework

The proposed EPG-motion framework demonstrates that rigid body and pulsatile motion leads to substantial changes in both temporal (Figure 3) and spatial (Figure 4) DW-SSFP signal profiles. Acquired experimental data agrees visually with forward simulations arising from the EPG-motion framework, demonstrating that the signal-forming mechanisms of DW-SSFP are highly sensitive to subject motion (Figures 7-9), independent of the readout. Without motion correction, diffusion coefficients are overestimated both theoretically (Figure 6a) and experimentally (Figure 10a), with the degree of misestimation additionally dependent on the diffusion gradient orientation (Figure 10a). Observed periodic changes in the DW-SSFP signal profile across individual voxels are

consistent with pulsatile brain motion (Figures 7 to 9), which cannot be addressed with volunteer compliance training or head restraints.

The proposed framework demonstrates that it's possible to estimate and correct for the impact of subject motion retrospectively based on timeseries data capturing the evolution of the DW-SSFP signal, yielding parameter estimates with consistent spatial contrast (Figures 9 and 10b) and agreement with complementary diffusion imaging methods (Figure 10c). Motion-corrected data using the proposed EPG-motion framework addresses the 'blue-bias' visible in earlier efforts to estimate tensors from motion-corrected DW-SSFP data[21], arising from the predominant motion-sensitivity of the DW-SSFP signal along the foot-head direction, which previously required spatial filtering to remove[21,22].

Motion Characterisation during Systole

The estimated $V(\mathrm{t})$ maps (Figure 9) display smooth and consistent contrast across the brain during diastole and systole. A notable exception during systole is the central brain region in the foot-head gradient dataset (Figure 9c) where subject motion is predicted to be largest. Visualisation of the DW-SSFP data (Figure 8c) demonstrates that the noisy motion parameter estimates are also associated with regions of low SNR, suggesting parameter misestimation during systole is a consequence of (1) noise, (2) parameter degeneracies associated with rapid signal changes in high-velocity tissue regions, or (3) a combination of the two.

To explore whether it is possible to reliably estimate $V(\mathrm{t})$ maps from DW-SSFP data acquired with a diffusion gradient along the foot-head axis, Supporting Information Figure S5 displays the equivalent spatial $V(\mathrm{t})$ maps estimated from the experimental b_0-equivalent ($\mathrm{b_{eff}} = 100\ \mathrm{s/mm^2}$) data, acquired for each of the 12 diffusion gradient orientations as part of the experimental acquisition. Importantly, b_0 data in DW-SSFP still requires application of a spoiler gradient (to achieve $2\pi \cdot n$ dephasing across the voxel), leading to a signal sensitive to subject motion. The b_0 spatial $V(\mathrm{t})$ maps (Supporting Information Figure S5) display consistent contrast with the $\mathrm{b_{eff}} = 500\ \mathrm{s/mm^2}$ $V(\mathrm{t})$ maps (Figure 9), without noisy velocity estimates observed when the diffusion gradient is oriented along the foot-head axis. Figure S6 displays an example DW-SSFP timeseries and $V(t)$ profile from this dataset in a central brain (thalamus) voxel, demonstrating a periodic profile consistent with the pulse oximeter estimates.

The $\mathrm{b_{eff}} = 500\ \mathrm{s/mm^2}$ dataset have intrinsically lower SNR and larger motion-induced signal changes versus the b_0-equivalent datasets. Figure S7 demonstrates that the equivalent DW-SSFP timeseries and $V(t)$ profile to Figure S6 for $\mathrm{b_{eff}} = 500\ \mathrm{s/mm^2}$ data. Here we observe an excellent fit to the DW-SSFP timeseries data, with rapid magnitude/phase changes in the DW-SSFP signal and large non-physical oscillatory velocity estimates during systole exceeding 3 mm/s. Whilst the signal-forming mechanisms of DW-SSFP create a nontrivial relationship between sequence parameters and the maximum velocity that can be reliably estimated, the excellent fit combined with a consistent, oscillatory velocity profile during systole is indicative of degeneracies in the relationship between $V(\mathrm{t})$ and the measured signal (i.e. distinct velocity profiles giving rise to similar signal estimates). Taken together, motion parameter estimation would be improved with informed initialisation of the temporal and spatial motion profile of the DW-SSFP signal, discussed further in the following section.

Despite this, misestimation of motion parameters during peak systole does not appear to significantly impact the estimation of D both experimentally (Figure 10) and in simulation (Figure 6 – see Supporting Information Figure S8 displays for the estimated $V(\mathrm{t})$ profiles from noiseless simulated data). In brief, the period of rapid velocity changes only forms a small part of the entire cardiac cycle. As only a single diffusion coefficient is estimated per voxel, sufficient DW-SSFP signal measurements during diastole should be sufficient to reliably estimate D, with methods to support parameter estimation described below.

Translation into a Generalised DW-SSFP Acquisition and Reconstruction Framework

In this work, the proposed EPG-motion framework was successfully applied to 2D, low-resolution single-shot DW-SSFP timeseries data. The acquired data is appropriate for validating the framework and understanding the origin of motion-induced imaging artefacts independent of the readout scheme, demonstrating that the signal forming mechanisms of DW-SSFP require motion estimates to be integrated into an EPG (or equivalent) signal model to characterise the temporal dynamics of the motion-corrupted signal. Furthermore, the degree of motion corruption in a voxel is shown to be modulated by the local diffusion coefficient (Figure 4 & Supporting

Information Figure S4), which should be simultaneously estimated or accounted for as part of any motion-reconstruction procedure. The simplified fitting approach (non-linear least-squares, single motion estimate per TR, no regularisation) implemented independently for each voxel did not enforce any prior knowledge or constraints on the motion profile, with smooth spatial distributions of $V(t)$ (Figure 9) arising naturally from the parameter estimation procedure.

When considering a 3D, segmented readout DW-SSFP sequence, the impact of subject motion on reconstructed images will be more severe due to the contribution of both the motion-sensitive DW-SSFP signal (investigated in this manuscript) and phase/magnitude inconsistencies between individual k-space segments. To establish approaches to address this, it can be first recognised that adjacent voxels share information about subject motion. When considering *rigid body* (e.g. subject translations and rotations), subject motion across the whole brain is simply characterised by six motion parameters ($\vec{v}_{x/y/z}$ and $\vec{\omega}_{x/y/z}$) and three additional parameters indicating the centre of origin of rotation along each spatial axis (required for estimating $\vec{X}_{x/y/z}$). For brain pulsatility, the motion profile is observed to be smoothly varying across the brain both spatially (Figure 9) and temporally (Figure 7), consistent with previous observations using complementary motion-estimation procedures.

Taken together, the proposed framework could be integrated into a motion-reconstruction procedure that performs simultaneous parameter estimation across voxels considering a smoothly varying (1) spatial and (2) temporal motion profile, substantially reducing the dimensionality of parameter estimation. As pulsatile brain motion should follow a consistent spatial and temporal profile across different cardiac cycles, velocity estimation could be integrated with information from complementary methods (e.g. phase contrast imaging[50], DENSE[48,51], Amplified MRI[49,52]) and combined with ECG/Pulse oximeter measurements acquired during DW-SSFP acquisition to regularise the fitting procedure. This information could be leveraged with sequences integrating navigators and non-cartesian readouts to establish motion-robust DW-SSFP acquisition schemes.

Software

The released software (available at github.com/BenjaminTendler/MotionCorrectionDWSSFP) provides a framework to investigate the impact of motion on the DW-SSFP signal, allowing for the forward simulation of temporal motion profiles for 1D, 2D and 3D imaging volumes, the resulting DW-SSFP signal, and estimation of motion parameters from DW-SSFP timeseries data. Scripts to replicate many of the figures presented in this manuscript are also provided.

Conclusion

We present a framework to characterise how rigid-body and pulsatile motion impact the DW-SSFP signal, finding consistent observations between the proposed framework, Monte Carlo simulations, and acquired experimental DW-SSFP data. We demonstrate that it is possible to estimate and correct for the impact of subject motion, with motion-corrected experimental DW-SSFP data displaying consistent contrast with DW-SE tensor estimates. The proposed framework is entirely open source, facilitating future investigations into the impact of motion on DW-SSFP acquisitions.

Acknowledgements

BCT is funded by a Sir Henry Wellcome Postdoctoral Fellowship (Wellcome Trust) [222829/Z/21/Z]. WW is funded by the Royal Academy of Engineering [RF\201819\18\92]. KLM is funded by a Wellcome Trust Senior Research Fellowship [224573/Z/21/Z]. This research was supported by the NIHR Oxford Health Biomedical Research Centre [NIHR203316]. The views expressed are those of the author(s) and not necessarily those of the NIHR or the Department of Health and Social Care. The Centre for Integrative Neuroimaging was supported by core funding from the Wellcome Trust [203139/Z/16/Z and 203139/A/16/Z].

This research was funded in whole, or in part, by the Wellcome Trust [222829/Z/21/Z, 224573/Z/21/Z, 203139/Z/16/Z, 203139/A/16/Z]. For the purpose of open access, the author has applied a CC BY public copyright licence to any Author Accepted Manuscript version arising from this submission.

Data Availability Statement

Software for the proposed EPG-motion framework, including scripts to replicate many of the findings presented in this manuscript, are available at github.com/BenjaminTendler/MotionCorrectionDWSSFP, SHA #2101cb09afa30d32d33ba0c4246a76725d601fe1.

Contributions Statement:

BCT designed the project; established the theory and developed the EPG-motion framework; optimised the DW-SSFP sequence parameters; implemented the sequences; performed pilot and subject scanning; performed all analysis; wrote the manuscript and produced all figures. **WW** developed the DW-SSFP sequence; and provided manuscript feedback. **KLM** contributed to the project design, providing guidance and feedback on the investigative pathway, theory, and findings; developed the DW-SSFP Monte Carlo simulation software; and provided manuscript feedback. **ATH** oversaw the experimental data acquisition, informing experimental design, providing guidance and feedback on the investigative pathway based on pilot data; modified the DW-SSFP sequence, enabling the acquisition of described experimental data and integrated pulse oximeter measurements; performed pilot and subject scanning; and provided manuscript feedback.

References

1. Le Bihan D. Intravoxel incoherent motion imaging using steady-state free precession. *Magn Reson Med*. 1988. 10.1002/mrm.1910070312
2. Merboldt KD, Hänicke W, Gyngell ML, Frahm J, Bruhn H. Rapid NMR imaging of molecular self-diffusion using a modified CE-FAST sequence. *J Magn Reson*. 1989. 10.1016/0022-2364(89)90170-4
3. Merboldt K, Bruhn H, Frahm J, Gyngell ML, Hänicke W, Deimling M. MRI of “diffusion” in the human brain: New results using a modified CE-FAST sequence. *Magn Reson Med*. 1989. 10.1002/mrm.1910090316
4. Kaiser R, Bartholdi E, Ernst RR. Diffusion and field-gradient effects in NMR Fourier spectroscopy. *J Chem Phys*. 1974. 10.1063/1.1681477
5. Stejskal EO, Tanner JE. Spin diffusion measurements: Spin echoes in the presence of a time-dependent field gradient. *J Chem Phys*. 1965. 10.1063/1.1695690
6. McNab JA, Jbabdi S, Deoni SCL, Douaud G, Behrens TEJ, Miller KL. High resolution diffusion-weighted imaging in fixed human brain using diffusion-weighted steady state free precession. *Neuroimage*. 2009. 10.1016/j.neuroimage.2009.01.008
7. McNab JA, Miller KL. Sensitivity of diffusion weighted steady state free precession to anisotropic diffusion. *Magn Reson Med*. 2008. 10.1002/mrm.21668
8. Tendler BC. Investigating time-independent and time-dependent diffusion phenomena using steady-state diffusion MRI. *Sci Rep*. 2025;15(1):3580.
9. Chenevert TL, Pipe JG. Effect of bulk tissue motion on quantitative perfusion and diffusion magnetic resonance imaging. *Magn Reson Med*. 1991;19(2):261-265.
10. Anderson AW, Gore JC. Analysis and correction of motion artifacts in diffusion weighted imaging. *Magn Reson Med*. 1994;32(3):379-387.
11. Chenevert TL, Pipe JG, Williams DM, Brunberg JA. Quantitative measurement of tissue perfusion and diffusion in vivo. *Magn Reson Med*. 1991;17(1):197-212.
12. Turner R, Le Bihan D. Single-shot diffusion imaging at 2.0 Tesla. *J Magn Reson*. 1990;86(3):445-452.
13. Turner R, Le Bihan D, Maier J, Vavrek R, Hedges LK, Pekar J. Echo-planar imaging of intravoxel incoherent motion. *Radiology*. 1990;177(2):407-414.
14. Wedeen VJ, Weisskoff RM, Poncelet BP. MRI signal void due to in-plane motion is all-or-none. *Magn Reson Med*. 1994;32(1):116-120.
15. Storey P, Frigo FJ, Hinks RS, et al. Partial k-space reconstruction in single-shot diffusion-weighted echo-planar imaging. *Magn Reson Med*. 2007;57(3):614-619.
16. Andersson JLR, Graham MS, Zsoldos E, Sotiropoulos SN. Incorporating outlier detection and replacement into a non-parametric framework for movement and distortion correction of diffusion MR images. *Neuroimage*. 2016;141:556-572.
17. Bosak E, Harvey PR. Navigator motion correction of diffusion weighted 3D SSFP imaging. *Magn Reson Mater Physics, Biol Med*. 2001;12:167-176.
18. Miller KL, Pauly JM. Nonlinear phase correction for navigated diffusion imaging. *Magn Reson Med*.

2003;50(2):343-353.
19. Jung Y, Samsonov AA, Block WF, et al. 3D diffusion tensor MRI with isotropic resolution using a steady-state radial acquisition. *J Magn Reson Imaging*. 2009;29(5):1175-1184.
20. McNab JA, Gallichan D, Miller KL. 3D steady-state diffusion-weighted imaging with trajectory using radially batched internal navigator echoes (TURBINE). *Magn Reson Med*. 2010;63(1):235-242.
21. O'Halloran RL, Aksoy M, Van AT, Bammer R. 3D isotropic high-resolution diffusion-weighted MRI of the whole brain with a motion-corrected steady-state free precession sequence. *Magn Reson Med*. 2013;70(2):466-478.
22. O'Halloran R, Aksoy M, Aboussouan E, Peterson E, Van A, Bammer R. Real-time correction of rigid body motion-induced phase errors for diffusion-weighted steady-state free precession imaging. *Magn Reson Med*. 2015;73(2):565-576.
23. Bieri O, Ganter C, Welsch GH, Trattnig S, Mamisch TC, Scheffler K. Fast diffusion-weighted steady state free precession imaging of in vivo knee cartilage. *Magn Reson Med*. 2012. 10.1002/mrm.23061
24. Miller KL, Hargreaves BA, Gold GE, Pauly JM. Steady-State Diffusion-Weighted Imaging of In Vivo Knee Cartilage. *Magn Reson Med*. 2004. 10.1002/mrm.10696
25. Zhang ZW, Song LJ, Meng QF, et al. High-resolution diffusion-weighted MR imaging of the human lumbosacral plexus and its branches based on a steady-state free precession imaging technique at 3T. *Am J Neuroradiol*. 2008;29(6):1092-1094.
26. Ehman RL, Felmlee JP. Adaptive technique for high-definition MR imaging of moving structures. *Radiology*. 1989;173(1):255-263.
27. Butts K, de Crespigny A, Pauly JM, Moseley M. Diffusion-weighted interleaved echo-planar imaging with a pair of orthogonal navigator echoes. *Magn Reson Med*. 1996;35(5):763-770.
28. Pipe JG. Motion correction with PROPELLER MRI: application to head motion and free-breathing cardiac imaging. *Magn Reson Med*. 1999;42(5):963-969.
29. Pipe JG. Multishot diffusion weighted FSE with PROPELLER. In: *Proceedings of the 9th Annual Scientific Meeting of ISMRM*. 2001.
30. Kim D hyun, Adalsteinsson E, Spielman DM. Simple analytic variable density spiral design. *Magn Reson Med*. 2003;50(1):214-219.
31. Liu C, Bammer R, Kim D hyun, Moseley ME. Self-navigated interleaved spiral (SNAILS): application to high-resolution diffusion tensor imaging. *Magn Reson Med*. 2004;52(6):1388-1396.
32. Chen N kuei, Guidon A, Chang HC, Song AW. A robust multi-shot scan strategy for high-resolution diffusion weighted MRI enabled by multiplexed sensitivity-encoding (MUSE). *Neuroimage*. 2013;72:41-47.
33. Mani M, Jacob M, Kelley D, Magnotta V. Multi-shot sensitivity-encoded diffusion data recovery using structured low-rank matrix completion (MUSSELS). *Magn Reson Med*. 2017;78(2):494-507.
34. Wansapura JP, Holland SK, Dunn RS, Ball Jr WS. NMR relaxation times in the human brain at 3.0 tesla. *J Magn Reson Imaging*. 1999;9(4):531-538.
35. Weigel M. Extended phase graphs: Dephasing, RF pulses, and echoes - Pure and simple. *J Magn Reson Imaging*. 2015. 10.1002/jmri.24619
36. Tendler BC. Theoretical framework to characterise motion artefacts arising from steady-state diffusion MRI. In: *European Society of Magnetic Resonance in Medicine & Biology (ESMRMB) Annual Scientific Meeting*. 2023:LB298.
37. Bloch F. Nuclear Induction. *Phys Rev*. 1946;70(7-8):460-474. 10.1103/PhysRev.70.460
38. Weigel M, Schwenk S, Kiselev VG, Scheffler K, Hennig J. Extended phase graphs with anisotropic diffusion. *J Magn Reson*. 2010;205(2):276-285.
39. Greitz D, Wirestam R, Franck A, Nordell B, Thomsen C, Ståhlberg F. Pulsatile brain movement and associated hydrodynamics studied by magnetic resonance phase imaging: the Monro-Kellie doctrine revisited. *Neuroradiology*. 1992;34:370-380.
40. Buxton RB. The diffusion sensitivity of fast steady-state free precession imaging. *Magn Reson Med*. 1993. 10.1002/mrm.1910290212
41. Jenkinson M, Beckmann CF, Behrens TEJ, Woolrich MW, Smith SM. FSL - Review. *Neuroimage*. 2012. 10.1016/j.neuroimage.2011.09.015
42. Hall MG, Alexander DC. Convergence and Parameter Choice for Monte-Carlo Simulations of Diffusion MRI. *IEEE Trans Med Imaging*. 2009. 10.1109/TMI.2009.2015756
43. Miller KL, McNab JA, Jbabdi S, Douaud G. Diffusion tractography of post-mortem human brains: Optimization and comparison of spin echo and steady-state free precession techniques. *Neuroimage*. 2012. 10.1016/j.neuroimage.2011.09.054

44. Ehses P. Open Source Software: mapVBVD. 2022. Accessed May 14, 2025. github.com/pehses/mapVBVD
45. Bilgic B, Polimeni JR, Wald LL, Setsompop K. Automated tissue phase and QSM estimation from multichannel data. In: *Proceedings of the 24th Annual Meeting of ISMRM.* 2016:2849.
46. Bilgic B. Open Source Software: SVD for reference-free coil combination at high field. 2022. Accessed May 14, 2025. martinos.org/~berkin/software.html
47. Ehses P, Brenner D, Stirnberg R, Pracht ED, Stöcker T. Whole-brain B1-mapping using three-dimensional DREAM. *Magn Reson Med*. 2019;82(3):924-934.
48. Adams AL, Kuijf HJ, Viergever MA, Luijten PR, Zwanenburg JJM. Quantifying cardiac-induced brain tissue expansion using DENSE. *NMR Biomed*. 2019;32(2):e4050.
49. Terem I, Younes K, Wang N, et al. 3D Quantitative-Amplified Magnetic Resonance Imaging (3D q-aMRI). *Bioengineering*. 2024;11(8):851.
50. Pelc NJ, Herfkens RJ, Shimakawa A, Enzmann DR, others. Phase contrast cine magnetic resonance imaging. *Magn Reson Q*. 1991;7(4):229-254.
51. Zhong X, Meyer CH, Schlesinger DJ, et al. Tracking brain motion during the cardiac cycle using spiral cine-DENSE MRI. *Med Phys*. 2009;36(8):3413-3419.
52. Holdsworth SJ, Rahimi MS, Ni WW, Zaharchuk G, Moseley ME. Amplified magnetic resonance imaging (aMRI). *Magn Reson Med*. 2016;75(6):2245-2254.